Global and Stochastic Analysis
Vol. 13 No. 2 (2026)

DOI: 10.64837/GSA.13.2.6

Received: 28th January 2026 *Revised: 02nd April 2026* *Accepted: 02nd May 2026*

A DATA-DRIVEN PHYSICS-INFORMED NEURAL NETWORK APPROACH FOR ANALYSIS OF POLLUTANT DISCHARGE CONCENTRATION IMPACT ON AN OSCILLATORY SURFACE

G. J. MANJULA, HAKEEM A. OTHMAN, S. SURESHA, HUSNIYAH ALZUBAIDI,
A. B. SATHISHA, C. G. JAGANNATHA, LAL SING NAIK*, AND K. C. JAGADEESHA

Abstract. Pollutant concentration analysis is essential for forecasting pollutant transport, assessing the processes of mixing and dilution in natural water bodies, and identifying possible ecological hazards. Because they provide light on how pollutants disperse in air or water under the influence of oscillatory movements, these models are crucial for ecological engineers creating efficient pollution control strategies. In view of this, the present examination explores the consequence of the magnetic field and pollutant concentration on the liquid flow across an oscillatory stretchable surface with a non-uniform heat source/sink effect. Additionally, the ordinary differential equations (ODEs) are numerically solved by utilizing the finite difference technique. Further, the physics-informed neural network approach is employed to evaluate the flow dynamics. Graphs illustrate the relative importance of different parameters on the concentration, thermal, and velocity profiles. The fluctuation of dimensionless time on the velocity profile is exhibited. The thermal profile upsurges as the Brownian motion parameter and thermophoretic parameter value increase. The concentration profile increases with the elevation of external pollutant source variations and thermophoretic parameter values.

Nomenclature:

Symbol	Description	Symbol	Description
Pr	Prandtl number	Nb	Brownian movement parameter
$\theta(y,t)$	Dimensionless temperature	$f(y,t)$	Dimensionless velocity
M	Magnetic parameter	λ	Pollutant external source parameter
μ	Dynamic viscosity	C_w	Wall concentration
A^* and B^*	Space and temperature-dependent internal heat generation/absorption coefficient	T_w	Wall temperature
ρ	Density	Sc	Schmidt number
$(\bar{x},\bar{y})$	Axis	D_B	Brownian diffusion coefficient
c_p	Specific heat	Cf_x	Skin friction
T_∞	Ambient temperature	b_3	Pollutant external source variation
T	Temperature	b	Stretching rate

2000 *Mathematics Subject Classification.* Primary: 65M99, 76Rxx; Secondary: 76Mxx, 35Q35.

Key words and phrases. Oscillatory stretching sheet; Magnetic field; Thermophoresis and Brownian motion; Non-uniform heat source/sink; Pollutant concentration.

*Corresponding author.

Symbol	Description	Symbol	Description
C_∞	Ambient concentration	α	Pollutant external source variation parameter
Sh_x	Sherwood number	S	The ratio of oscillation frequency to extension rate
k	Thermal conductivity	$\chi(y,t)$	Dimensionless concentration
(u,v)	Velocity components	τ	Dimensionless time
Nt	Thermophoretic parameter	Re	Reynolds number
ω	Angular velocity	B_0	Magnetic field
C	Concentration	Nu_x	Nusselt number
t	Time	q'''	Non-uniform heat source/sink coefficient
Q	Pollutant source strength		

1. Introduction

Boundary layer motion evaluation with heat and mass transmission via a stretchy sheet has captivated significant interest from academics and engineers due to its applications in several industrial and manufacturing processes. The sheet may sometimes be stretched and show recurring oscillations across its two-dimensional plane. This phenomenon, which is reliant on time enables the examination of various characteristics of liquid motion at diverse points in time. The motion of the third-grade liquid via an oscillatory SS with the significance of radiation was explained by Ali et al. [4]. Utilising the spectral approach, Mkhatshwa et al. [20] studied the fluid stream via an oscillatory stretchable surface (OSS). The heat transmission and liquid stream across an OSS were delineated by Ali et al. [5]. The homotopy tactic was utilised by Abbas et al. [1] to examine the liquid stream over an OSS. The stream of fluid via an OSS was deliberated by Srilatha et al. [29]. The electrically conductive liquids and their electromagnetic interactions are studied in magnetohydrodynamics (MHD), a field with many real-world applications. Particular uses include boundary layer effects, nuclear reactor cooling, bearings, and MHD power generation. The fluid's interaction with an electrically conductive fluid and a magnetic field (MF) affects these applications. Electrically conductive fluids and magnetic fields have a significant impact on hydromagnetic boundary layers. These days, a number of studies increase the surface in transverse flow when an MF is present in order to address the boundary layer stream problem. The effect of MF on the hybrid nanoliquid flow over an stretching sheet (SS) was assessed by Varsha et al. [31]. Osaci and Cacciola [23] investigated the Brownian relaxation of unsteady magnetic nanoliquids using a semi-analytical model. Mohapatra et al. [21] studied the consequence of size diversity on MF adjustable architectures in magnetic nanofluids, including superparamagnetic nanoparticles. Daniel et al. [7] examined the stream of fluid across the stretching sheet with the consequence of an MF. Goud and Aparna [8] analyzed the liquid flow via a vertical plate under the MF impact.

Heat transport is vital in many residential, industrial, technical, and commercial sectors. Heat must be efficiently and effectively supplied, withdrawn, or transferred from one process to another at all sites to maintain the current state. There are several real-world uses for researching the industrial sector's flow and internal heat production and absorption. Heat generation and absorption substantially effect the thermal convection process when a considerable temperature disparity exists between the surface fluid and the surrounding liquid. Heat production affects the deposition rate of nuclear reactors, semiconductor wafers and electronic chips. Many theoretical investigations on heat transfer and fluid flow issues assume that internal heat production or absorption is constant, varies with space, or varies with temperature (non-uniform heat source/sink (HSS)). Manvi et al. [18] deliberated the effect of non-uniform HSS on the stream of fluid stream via an expandable surface. The motion of nanoliquid past an SS with the consequence of non-uniform HSS was analyzed by Thumma et al. [30]. The attributes of non-uniform HSS on the nanofluid stream through the stretchable cylinder were exemplified by Song et al. [28]. The temperature analysis of the Sutterby liquid stream via a stretching sheet with non-uniform HSS consequence was examined by Hussain et al. [11]. The consequence of non-uniform HSS on the liquid stream across a gyrating disk was inspected by Kumar et al. [13]. The force that various suspended particles respond to as a result of a temperature differential is known as thermophoresis or thermodiffusion. Brownian motion denotes the inconsistent movement shown by particles dispersed in a liquid medium. There are several uses in nanotechnology, electrical systems, astrophysics, plasma research, etc. Thermophoresis and Brownian motion (TBM) significantly influence mass and heat transmission in fluids. Munjam et al. [22] studied the influence of TBM on the stream of nanofluid over a curved stretched sheet. Saghir and Rahman [25] investigated the nanoliquid flow outside the surface with TBM. Soomro et al. [27] pondered the motion of fluid over the SS under the effect of the TBM. The impact of TBM on the motion of nanofluid via a nonlinear surface was researched by Reddy et al. [12]. Ullah and Bilal [33] elucidated the transfer of heat characteristics in the nanofluid flow across an extending surface with TBM impact.

Early identification is crucial for swift and suitable response in several liquid pollution events (including air or water contamination). The harmful impacts of water pollution on the environment also add to the air pollution's hazardous effects on human health. Establishing early warning systems is essential for detecting or predicting pollution levels to reduce or prevent downstream damage. It is essential to formulate accurate methodologies for predicting the magnitude of the pollution impact. Makinde and Chinyoka [17] evaluated the pollutant dispersion examination of the fluid stream via the cylindrical surface. A thorough description of how pollutant concentration and HSS affect the liquid motion via a stretchable sheet was given by Yaseen et al. [34]. Lim et al. [16] noted the impact of chemical processes and turbulence dispersal on producing local concentrations of pollution dispersion. Vinutha et al. [32] studied the liquid motion through a convergent channel with respect to the concentration of waste discharge. Albalawi et al. [3] examined the fluid flow around the cylinder in connection with pollution concentration levels.

Differential equations may be solved using advanced machine-learning techniques called physics-informed neural networks (PINNs). It provides precise and physically consistent predictions by fusing the representational capability of neural networks with the physical principles that govern a system. Initially, the domain is discretized using collocation to solve the equations, and this method uses a neural network to comprehend the system's fundamental physics to forecast its behaviour. PINNs are used to solve various real-world problems and provide a more efficient and accurate approach. Lagaris et al. [14] used the neural network approach to examine the Boundary Value Problem (BVP). These days, complicated nonlinear equation systems are solved using PINN, which has grown in popularity over time. An extensive overview of the PINN and its use in fluid flow studies was given by Sharma et al. [26]. Li et al. [15] examined fluid behaviour by using neural networks to solve the conservative rules. The results indicated that the proposed model may be utilised to predict thermal performance. According to Bhaumik et al. [6], comparing the performance of data-driven black box models with PINN enables accurate forecasting of nanofluids' thermal conductivity. Electro-osmosis-driven flows were the subject of Merdasi et al. [19] study. PINN is used to anticipate the pressure of these flows, and the outcomes are compared with the finite volume scheme.

The present examination examines the consequence of pollutant concentration on fluid motion via an oscillatory SS with MF. The impacts of TBM and non-uniform HSS are also considered. Industrial and environmental engineering find great uses for the analysis of liquid stream over an OSS with pollution concentration. In manufacturing, such models assist in maximising coating and extrusion processes where fluids, including impurities or additives, interact with moving surfaces, including in polymer processing, glass making, and metal rolling. They are also very important in medical technology for the delivery of drugs with oscillating surfaces. Knowing heat and mass transmission in such flows improves the chemical processing industry and the thermal management system efficiency. Examining the fluid motion and transmission of waste items in stretched sheets may help to enhance effective waste removal and pollution prevention measures. The partial differential equations (PDEs) are converted into ODEs using similarity variables. Additionally, the ODEs are solved numerically employing the finite difference method (FDM). Moreover, the PINN approach is used to analyze the fluid flow dynamics. A visual depiction shows how various factors affect the involved profiles.

2. Mathematical Formulation

In the presence of an MF, the liquid motion past an OSS is examined. The effect of pollutant concentration, non-uniform HSS and TBM is considered. The sheet is presumed to change periodically with velocity $u_w = \bar{x} b \sin \omega t$ in which t is the time, b is the stretching rate, and ω denotes the angular velocity. The sheet maintains the space $\bar{y} > 0$ and is positioned in the $\bar{x}$ plane. The MF B_0 of uniform strength is applied. Let (u, v) be the velocity components in $(\bar{x}, \bar{y})$ directions (See Figure 1). C and T are taken as the concentration and temperature. The governing equations are as follows (see [2, 4, 17, 24]):

$$\frac{\partial u}{\partial \bar{x}} + \frac{\partial v}{\partial \bar{y}} = 0, \tag{1}$$

$$\frac{\partial u}{\partial \bar{y}} v + \frac{\partial u}{\partial t} + \frac{\partial u}{\partial \bar{x}} u = \nu \frac{\partial^2 u}{\partial \bar{y}^2} - \frac{\sigma}{\rho} B_0^2 u, \tag{2}$$

$$u \frac{\partial T}{\partial \bar{x}} + \frac{\partial T}{\partial t} + v \frac{\partial T}{\partial \bar{y}} = \frac{k}{(\rho c_p)} \frac{\partial^2 T}{\partial \bar{y}^2} + \varsigma_1 \left(\left(\frac{\partial T}{\partial \bar{y}} \right)^2 \frac{D_T}{T_\infty} + D_B \frac{\partial T}{\partial \bar{y}} \frac{\partial C}{\partial \bar{y}} \right) + \frac{q'''}{(\rho c_p)}, \tag{3}$$

$$v \frac{\partial C}{\partial \bar{y}} + \frac{\partial C}{\partial t} + u \frac{\partial C}{\partial \bar{x}} = D_B \frac{\partial^2 C}{\partial \bar{y}^2} + Q \exp\left(b_3 \left(C - C_\infty \right) \right) + \frac{D_T}{T_\infty} \frac{\partial^2 T}{\partial \bar{y}^2}. \tag{4}$$

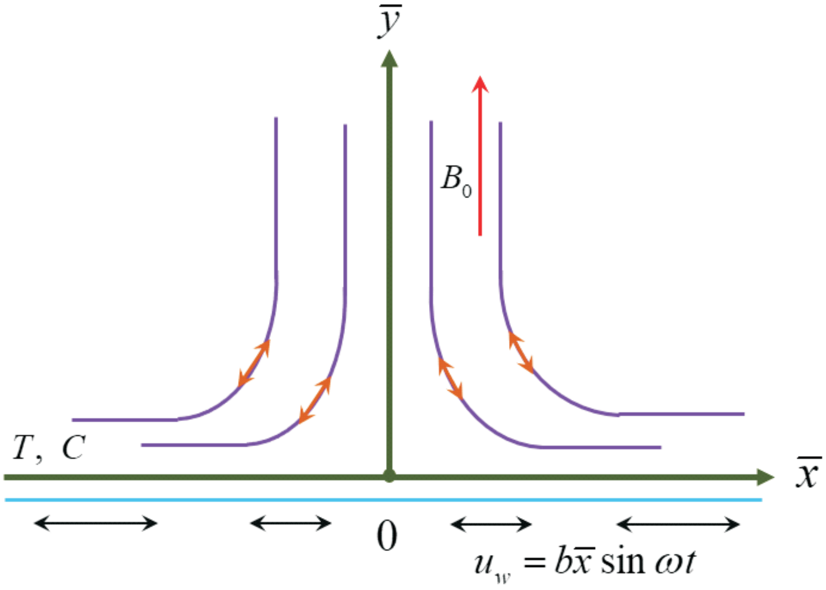

Figure 1. Geometry of the problem.

The boundary circumstances are given as follows,

$$u = u_w = \bar{x} b \sin\omega\, t,\quad T = T_w,\ \ C = C_w, v = 0\ \ \text{at}\ \ \bar{y} = 0,\ \ \tau > 0,$$

$$T \to T_\infty,\ u = 0, C \to C_\infty \quad \text{as} \quad \bar{y} \to \infty. \tag{5}$$

The similarity variables are introduced as,

$$u = b\bar{x}\, f_y(y,\tau),\ \ \chi(y,\tau) = \frac{C - C_\infty}{C_w - C_\infty}\ ,\ \ \tau = \omega\, t\ ,\ \ y = \sqrt{\frac{b}{\nu}}\,\bar{y},$$

$$v = -\sqrt{b\,\nu} f(y,\tau),\ \ \theta(y,\tau) = \frac{T - T_\infty}{T_w - T_\infty}. \tag{6}$$

The non-uniform HSS q''' which can be signified as, (see [2])

$$q''' = \left(\frac{k\, u_w}{\bar{x}\,\nu}\right)[f_y(y,\tau)(T_w - T_\infty)A^* + (T - T_\infty)B^*].$$

It is well known that $B^* > 0$ and $A^* > 0$ resemble to interior heat production while $B^* < 0$ and $A^* < 0$ resemble to internal heat absorption.
The solved equations are as follows:

$$f_{yyy} - (f_y)^2 - S f_{y\,\tau} + f\, f_{yy} - M\, f_y = 0, \tag{7}$$

$$\theta_{yy} + \Pr(Nb\,\theta_y\,\chi_y + f\theta_y - S\theta_\tau + Nt(\theta_y)^2) + \sin\tau(A^* f_y + B^*\theta) = 0, \tag{8}$$

$$\chi_{yy} + Sc(-S\chi_\tau + f\chi_y + \lambda\exp(\alpha\,\chi)) + \frac{Nt}{Nb}\theta_{yy} = 0. \tag{9}$$

The reduced boundary circumstances are attained as,

$$f_y(0,\tau)=\sin\tau,\ \ \theta(0,\tau)=1,\ \ f(0,\tau)=0,\ \ \chi(0,\tau)=1,$$
$$f_y(\infty,\tau)=0,\ \ \theta(\infty,\tau)=0,\ \ \chi(\infty,\tau)=0. \tag{10}$$

Where, $\Pr=\frac{\nu(\rho c_p)}{k}$, $Sc=\frac{\nu}{D_B}$, $S=\frac{\omega}{b}$, $\tau=\omega t$, $M=\frac{\sigma}{\rho b}B_0^2$, $\lambda=\frac{Q}{b(C_w-C_\infty)}$, $\alpha=b_3(C_w-C_\infty)$, $Nb=\varsigma_1\frac{D_B(C_w-C_\infty)}{\nu}$, $Nt=\varsigma_1\frac{D_B(T_w-T_\infty)}{T_\infty\,\nu}$.

The physical quantities are represented as,

$$C_{fx}=\frac{1}{\mathrm{Re}^{1/2}}f_{yy}(0,\tau),\ \ \frac{Nu_x}{\mathrm{Re}^{1/2}}=-\theta_y(0,\tau),\ \ \frac{Sh_x}{\mathrm{Re}^{1/2}}=-\chi_y(0,\tau) \tag{11}$$

3. Numerical Procedure

The FDM was one of the initial approaches employed for the numerical resolution of differential equations, particularly utilised for solving the differential form of governing equations. The procedure entails employing a Taylor series expansion to discretise the resultant components of the variable flow. The procedure entails discretising the resultant components of the variable flow through a Taylor series expansion. By employing forward difference (FD) approximations, we converted ODEs and boundary conditions into FD equations, as seen below (refer to [9, 10]). The equations (7) to (9) are simplified in conjunction with the boundary conditions.

$$\frac{\varsigma_{i+3}^n-3\varsigma_{i+2}^n+3\varsigma_{i+1}^n-\varsigma_i^n}{h_i^3}+\varsigma_i^n\,\frac{\varsigma_{i+2}^n+\varsigma_i^n-2\varsigma_{i+1}^n}{h_i^2}-(S)\,\frac{\varsigma_{i+1}^{n+1}-\varsigma_{i+1}^n-\varsigma_i^{n+1}+\varsigma_i^n}{h_ih_n}$$
$$-\left(\frac{\varsigma_{i+1}^n-\varsigma_i^n}{h_j}\right)^2-M\,\frac{\varsigma_{i+1}^n-\varsigma_i^n}{h_j}=0, \tag{12}$$

$$\frac{\Theta_{i+2}^n+\Theta_i^n-2\Theta_{i+1}^n}{h_i^2}+\sin\tau\left(A^*\frac{\varsigma_{i+1}^n-\varsigma_i^n}{h_j}+B^*\Theta_i^n\right)$$
$$+\Pr\left(\begin{array}{c}\varsigma_i^n\left(\dfrac{-\Theta_i^n+\Theta_{i+1}^n}{h_i}\right)-S\left(\dfrac{\Theta_i^{n+1}-\Theta_i^n}{h_n}\right)+Nt\left(\dfrac{-\Theta_i^n+\Theta_{i+1}^n}{h_i}\right)^2\\ +Nb\left(\dfrac{-\Theta_i^n+\Theta_{i+1}^n}{h_i}\right)\dfrac{\Delta_{i+1}^n-\Delta_i^n}{h_i}\end{array}\right)=0, \tag{13}$$

$$\frac{\Delta_{i+2}^n-2\Delta_{i+1}^n+\Delta_i^n}{h_i^2}+\frac{Nt}{Nb}\left(\frac{\Theta_{i+2}^n+\Theta_i^n-2\Theta_{i+1}^n}{h_i^2}\right)$$
$$+Sc\left(-S\left(\frac{\Delta_i^{n+1}-\Delta_i^n}{h_n}\right)+\varsigma_i^n\frac{\Delta_{i+1}^n-\Delta_i^n}{h_i}+\lambda\exp\left(\alpha\,\Delta_i^n\right)\right)=0. \tag{14}$$

The reduced boundary conditions are converted as,

$$\frac{\varsigma_1^n-\varsigma_0^n}{h_0}=\sin\tau,\ \ \varsigma_0^n=0,\ \ \Theta_0^n=1,\ \ \Delta_0^n=1,$$
$$\frac{\varsigma_{i+1_\infty}^n-\varsigma_{i_\infty}^n}{h_\infty}=0,\ \ \Theta_\infty^n=0,\ \ \Delta_\infty^n=0. \tag{15}$$

4. Physics informed neural network (PINN)

The neural network is modeled after the interconnections of neurons in the human brain, which serve as the foundation for this methodology. PINN provides a cutting-edge machine learning approach designated to overcome the difficulty in solving PDEs. A loss function must be minimised throughout the learning process in order to train a PINN. Boundary constraints and PDE residuals assessed at certain collocation locations within the domain are represented by terms in this loss function. To uphold the underlying physical rules and provide consistent predictions throughout the solution space, these collocation points are thoughtfully selected and positioned. The incorporation of physical concepts into neural network training via residual formulations is a fundamental characteristic of PINNs. To include the basic physics in the network design and get precise answers, equation (16) is used. The PINN efficiently solves the governing PDEs by minimising the mean squared error (MSE) loss function, which is specified in equation (17) and reflects the total loss evaluation.

$$
\begin{aligned}
Eq1_{Loss} &= \frac{1}{Col}\sum_{w=0}^{Col} \| f_{yyy}(y_w,\tau_w) + f(y_w,\tau_w)\, f_{yy}(y_w,\tau_w) - (f_y(y_w,\tau_w))^2 \\
&\quad - S f_{y\,\tau}(y_w,\tau_w) - M\, f_y(y_w,\tau_w)\|^2, \\
Eq2_{Loss} &= \frac{1}{Col}\sum_{w=0}^{Col} \| \Pr(f(y_w,\tau_w)\theta_y(y_w,\tau_w) - S\theta_\tau(y_w,\tau_w) + Nt\,(\theta_y(y_w,\tau_w)\,)^2 \\
&\quad + Nb\,\theta_y(y_w,\tau_w)\,\chi_y(y_w,\tau_w)) + \sin\tau(A^* f_y(y_w,\tau_w) + B^*\theta(y_w,\tau_w)) + \theta_{yy}(y_w,\tau_w)\|^2 \\
Eq3_{Loss} &= \frac{1}{Col}\sum_{w=0}^{Col} \Bigg\| \chi_{yy}(y_w,\tau_w) + Sc(-S\chi_\tau + f(y_w,\tau_w)\chi_y(y_w,\tau_w) + \lambda\exp(\alpha\,\chi(y_w,\tau_w))) \\
&\quad + \frac{Nt}{Nb}\theta_{yy}(y_w,\tau_w)\Bigg\|^2,
\end{aligned}
\tag{16}
$$

$$
Loss_{total} = Eq1_{Loss} + Eq2_{Loss} + Eq3_{Loss} + Bc_{Loss} \tag{17}
$$

5. Results and discussion

The TBM impact on liquid flow over an OSS with non-uniform HSS and pollutant concentration is designated mathematically. Numerical calculations are utilized to understand the influence of numerous factors on the $f_y(y,\tau)$, $\theta(y,\tau)$, and $\chi(y,\tau)$ fields. We identified the many aspects effecting the $f_y(y,\tau)$, $\theta(y,\tau)$, and $\chi(y,\tau)$ profiles in the graphs and obtained the necessary outcomes for the viscous liquid.

Figures 2(a-d) illustrates the outcome of M on the $f_y(y,\tau)$ with respect to time at different distances (a) $y = 0.2$ (b) $y = 0.5$ (c) $y = 1$ (d) $y = 2$ from the surface of the sheet. It is detected that when M values increase, the velocity's magnitude decreases. This might be because of the Lorentz force, a retarding force introduced by the MF that

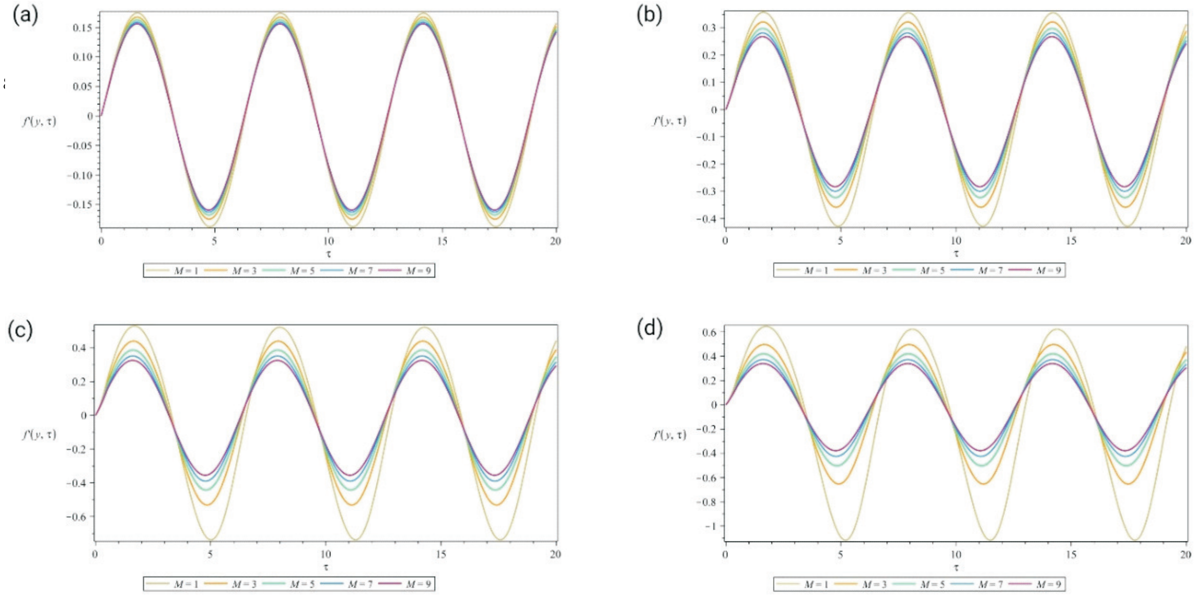

FIGURE 2. Consequence of M on $f_y(y,\tau)$ (a) $y = 0.2$ (b) $y = 0.5$ (c) $y = 1$ (d) $y = 2$.

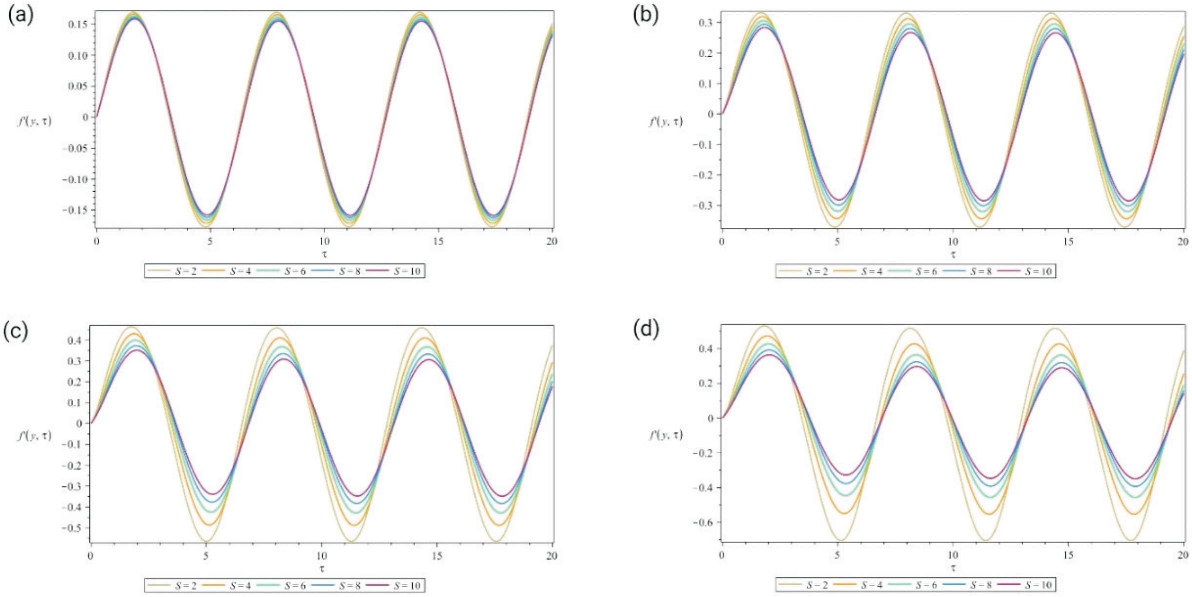

FIGURE 3. Consequence of S on $f_y(y,\tau)$ (a) $y = 0.2$ (b) $y = 0.5$ (c) $y = 1$ (d) $y = 2$.

serves as a flow barrier. Moreover, it is observed that velocity upsurges when the distance from the sheet increases from 0.2 to 2, as seen in Figures 2(a) to 2(d). Figures 3(a) to 3(d) shows the impact of S on the $f_y(y,\tau)$ with respect to time at different distances (a) $y = 0.2$ (b) $y = 0.5$ (c) $y = 1$ (d) $y = 2$ from the surface of the sheet. Here, the

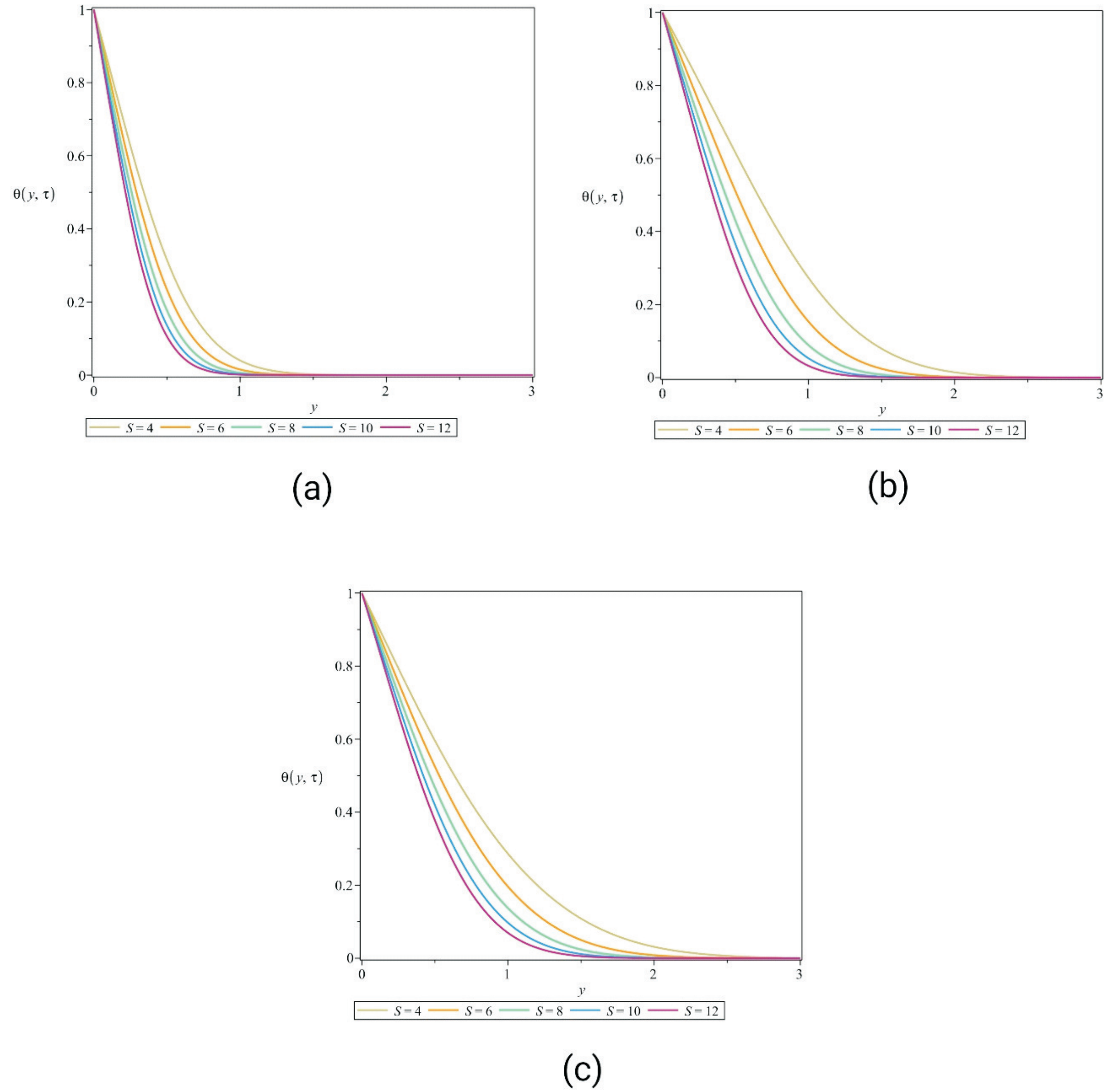

Figure 4. Consequence of S on $\theta(y,\tau)$ (a) $\tau=\pi$ (b) $\tau=2\pi$ (c) $\tau=3\pi$.

velocity declines for increasing values of S. An increase in S causes a substantial phase shift and an enhancement in oscillation amplitude, subsequent in a decrease in $f_y(y,\tau)$. Moreover, it is observed that velocity rises when the distance from the sheet upsurges from 0.2 to 2, as seen in Figures 3(a) to 3(d).

Effect of S on $\theta(y,\tau)$ with respect to different time periods (a) $\tau=\pi$ (b) $\tau=2\pi$ (c) $\tau=3\pi$ are shown in Figures 4(a) to 4(c). In this case, the thermal profile diminishes

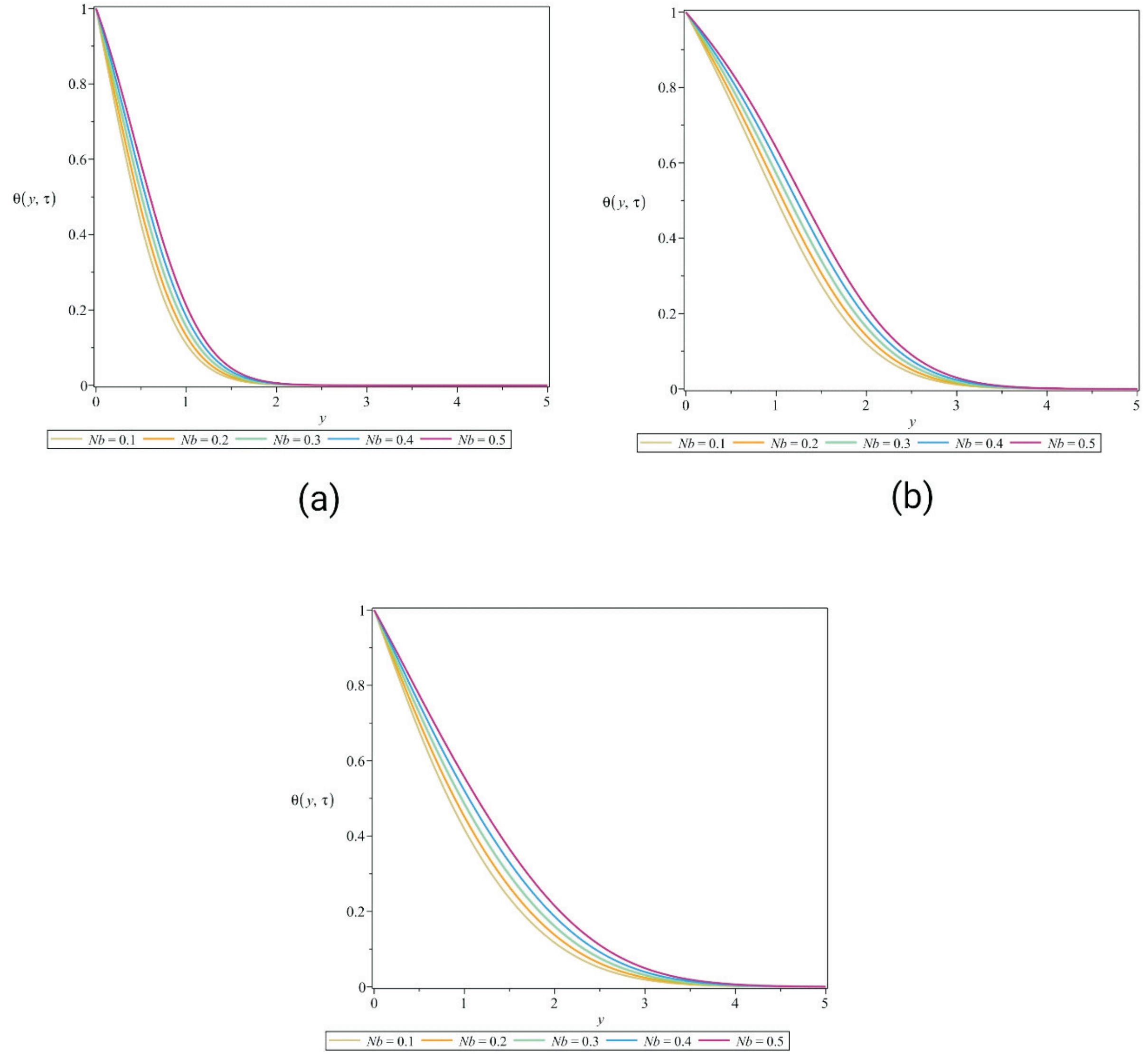

(a)

(b)

(c)

FIGURE 5. Consequence of Nb on $\theta(y, \tau)$ (a) $\tau = \pi$ (b) $\tau = 2\pi$ (c) $\tau = 3\pi$.

as S increases. When the ratio of the fluctuation rate to the extending rate is large, the fluctuating frequencies of the sheet rise faster than the stretching rate. This might result in improved mixing of fluid around the sheet. The $\theta(y, \tau)$ is often reduced by rapid oscillations because they enhance fluid mixing, promote heat dissipation, and lower the liquid's temperature. Furthermore, it is evident from Figures 4(a) to 4(c) that the thermal amplitude is higher close to the oscillatory surface than it is further away. The

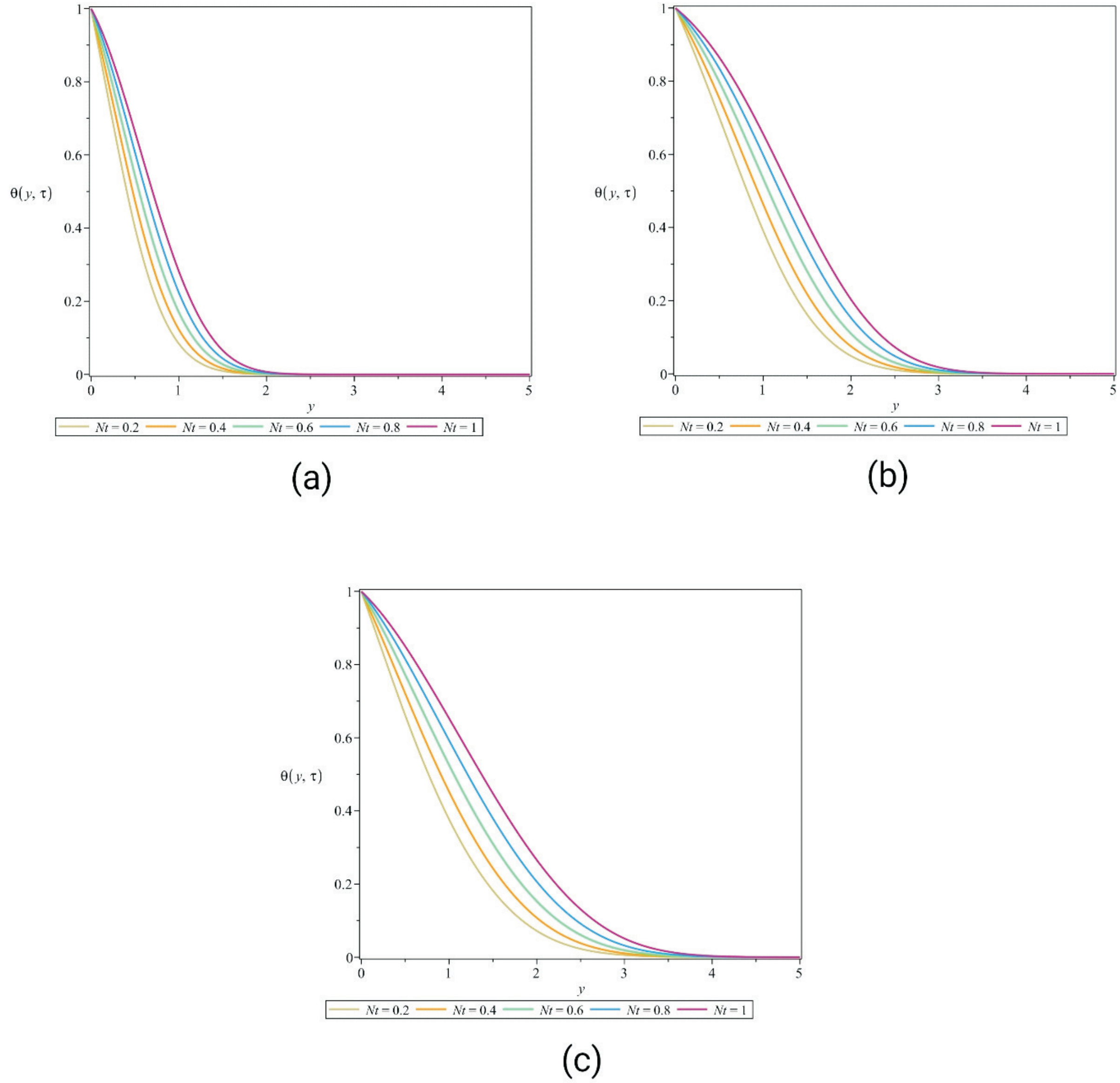

Figure 6. Consequence of Nt on $\theta(y,\tau)$ (a) $\tau=\pi$ (b) $\tau=2\pi$ (c) $\tau=3\pi$.

temperature decreases with increasing time periods away from the surface and almost disappears (gets closer to zero) for bigger time period values.

Impact of Nb on $\theta(y,\tau)$ with respect to different time periods (a) $\tau=\pi$ (b) $\tau=2\pi$ (c) $\tau=3\pi$ are shown in Figures 5(a) to 5(c). Here, the upsurge in Nb upsurges the $\theta(y,\tau)$ for all three cases. The temperature decreases with increasing time period away from the surface and almost disappears (gets closer to zero) for bigger time period values. This boundary layer's thickness and behaviour are influenced by the Nb. Because of

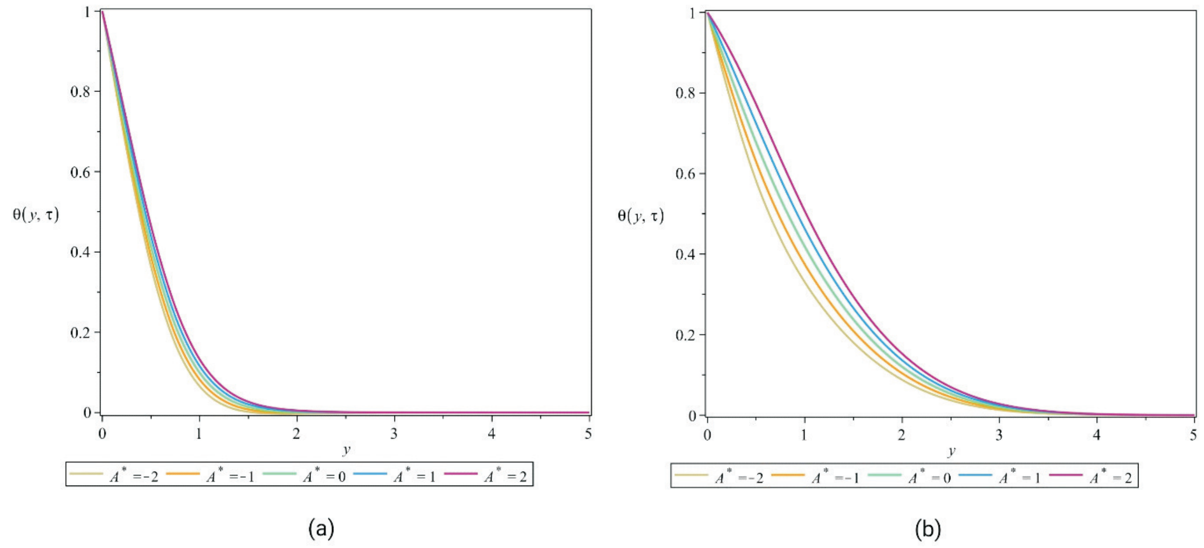

FIGURE 7. Consequence of A^* on $\theta(y,\tau)$ (a) $\tau=\pi$ (b) $\tau=3\pi$.

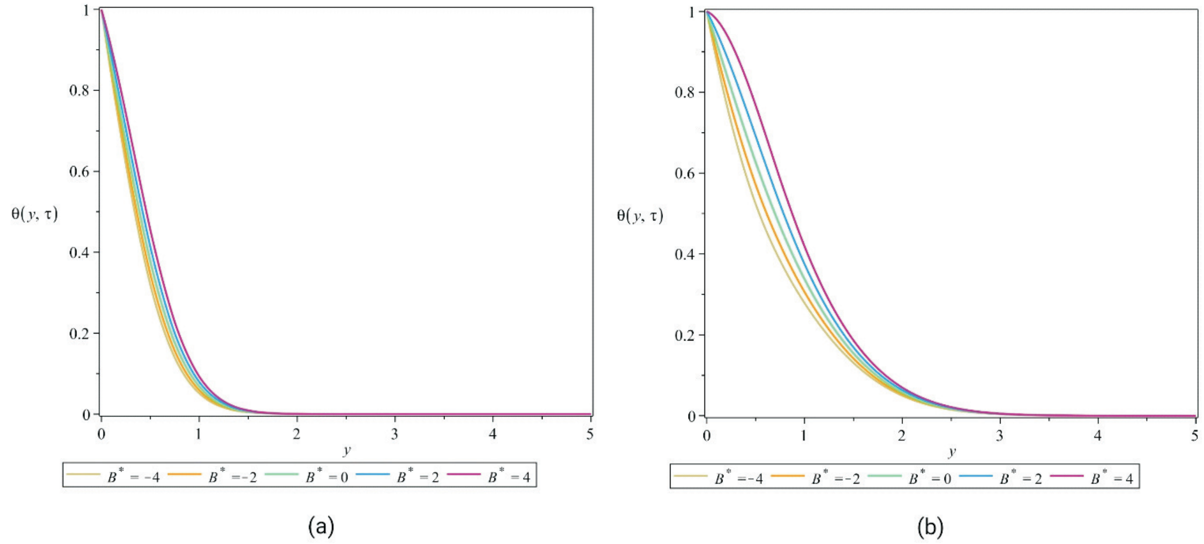

FIGURE 8. Consequence of B^* on $\theta(y,\tau)$ (a) $\tau=\pi$ (b) $\tau=3\pi$.

enhanced mixing and thermal diffusion within the liquid, a higher Nb may lead to a thinner boundary layer and a quicker heat exchange between the fluid and the stretched sheet. A longer length of time suggests a slower rate of oscillation for the stretched sheet. Therefore, the amount of heat transport between the liquid and the stretched sheet drops. The stretching sheet spends more time either entirely constricted or fully extended before changing direction when oscillations are less frequent. Temperature drops because there

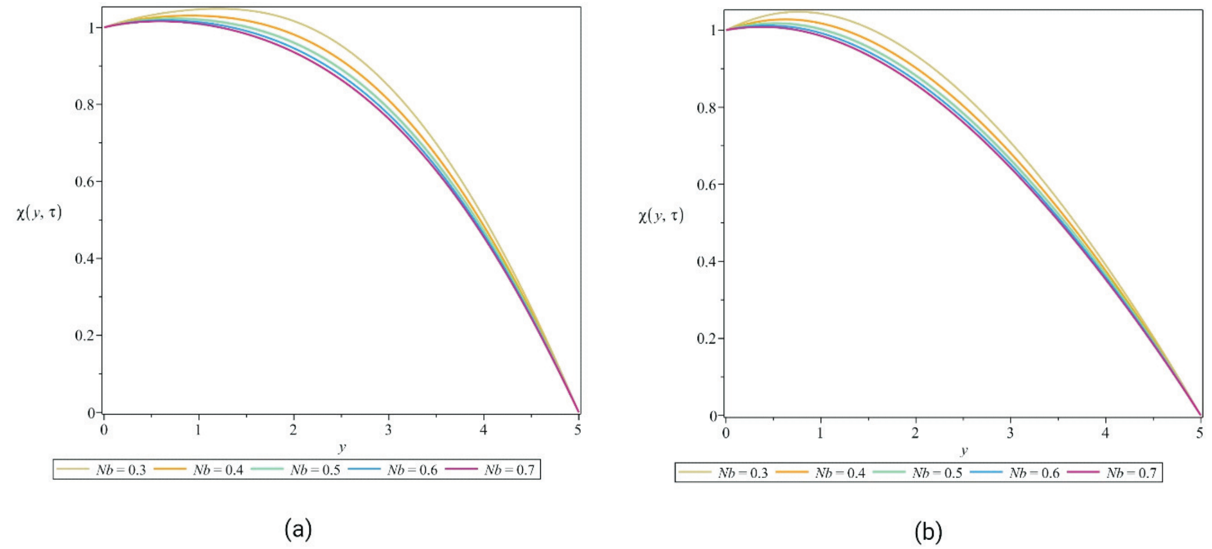

(a) (b)

FIGURE 9. Consequence of Nb on $\chi(y, \tau)$ (a) $\tau = 2\pi$ (b) $\tau = 3\pi$.

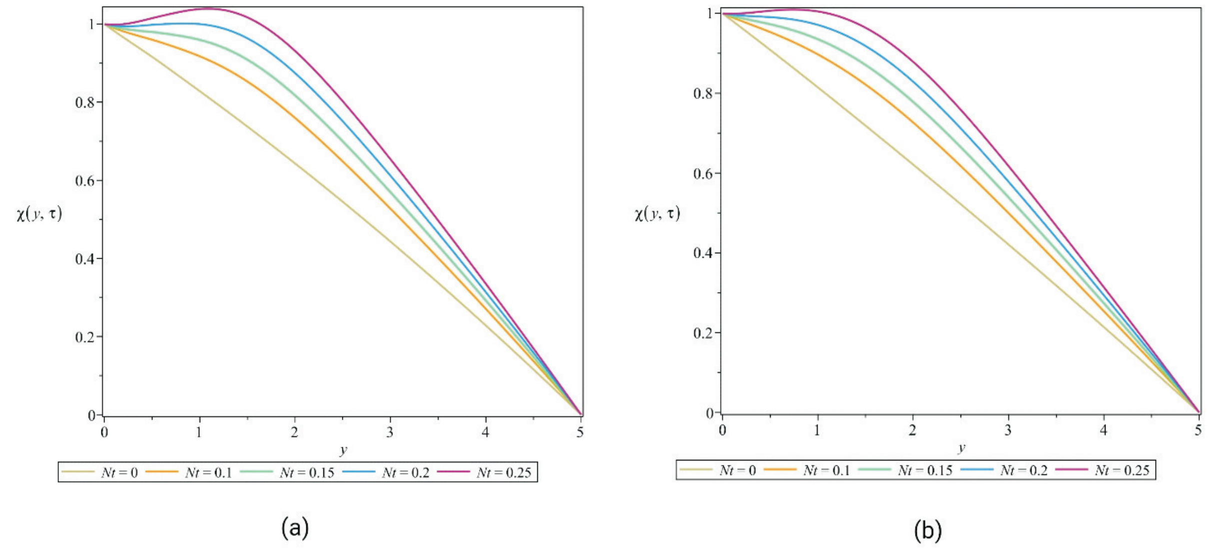

(a) (b)

FIGURE 10. Consequence of Nt on $\chi(y, \tau)$ (a) $\tau = 2\pi$ (b) $\tau = 3\pi$.

is less heat transmission between the sheet and the fluid during these prolonged times at extreme locations. Figures 6(a) to 6(c) explores the effect of Nt on $\theta(y, \tau)$ with respect to different time periods (a) $\tau = \pi$ (b) $\tau = 2\pi$ (c) $\tau = 3\pi$. Here, the escalation in Nt upsurges the $\theta(y, \tau)$ for all three cases. Additionally, it is evident from Figures 6(a) to 6(c) that the thermal profile is bigger close to the oscillatory surface than it is

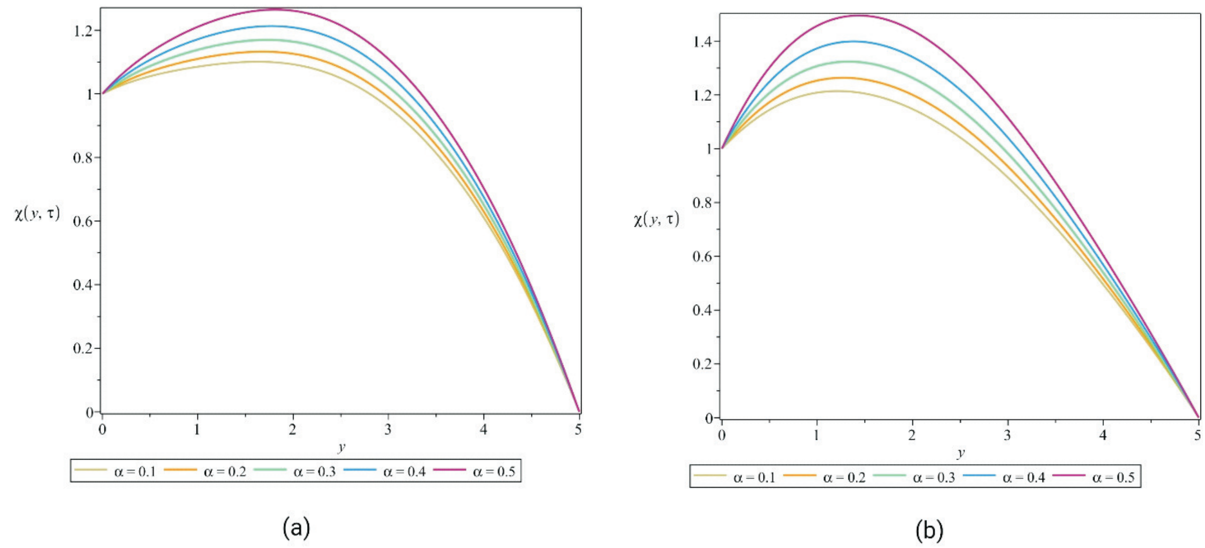

FIGURE 11. Consequence of α on $\chi(y,\tau)$ (a) $\tau = 2\pi$ (b) $\tau = 3\pi$.

farther away. The temperature decreases and, for bigger time period values, virtually approaches zero as the time period rises from the surface. The temperature progressively approaches zero for longer periods of time as the particles disperse throughout the fluid due to the augmented motion of particles away from the surface brought on by the rise in the thermophoresis parameter. Figures 7(a) to 7(b) displays the behaviour of $\theta(y,\tau)$ for numerous values of A^* with (a) $\tau = \pi$ and (b) $\tau = 3\pi$. The rise in A^* intensifies the $\theta(y,\tau)$. It is evident that the temperature boundary layer produces energy, which reasons the $\theta(y,\tau)$ to rise with increases in A^*. Figures 8(a) to 8(b) illustrates influence of B^* on the $\theta(y,\tau)$ for (a) $\tau = \pi$ and (b) $\tau = 3\pi$. These figures show that as B^* (>0) values rise, energy is released, leading to an increase in temperature for both $\tau = \pi$ and $\tau = 3\pi$. Conversely, when B^* (<0) values fall, energy is absorbed, resultant in a large reduction in temperature inside the boundary layer. Influence of Nb on $\chi(y,\tau)$ with respect two different conditions (a) $\tau = 2\pi$ and (b) $\tau = 3\pi$ is displayed in Figures 9(a) to 9(b). Here, inclined Nb decreases the concentration profile. Moreover, similar behaviour is detected for both the cases. Since it first showed up in the dimensionless concentration equation as $1/Nb$, where it causes a drop-in concentration profile. Nb often arises from the interaction with nanoparticles, which is associated with an increase in Brownian motion. Effect of Nt on $\chi(y,\tau)$ with respect two different conditions (a) $\tau = 2\pi$ and (b) $\tau = 3\pi$ is displayed in Figure 10 (a)-(b). Here, the inclined Nt increases the concentration profile. Moreover, similar behaviour is detected for both the cases. The consequence of α on $\chi(y,\tau)$ with respect two different conditions (a) $\tau = 2\pi$ and (b) $\tau = 3\pi$ is shown Figure11 (a)-(b). Here, the improvement in values of α increases the $\chi(y,\tau)$ for both the instances. Moreover, similar behaviour is detected for both the cases.

Figure 12 portrays the significance of Nb and S on Nu_x. The Nu_x declines for S and Nb due to the reduced thermal transport intensity. An advancement in S persuades a noteworthy phase shift and a growth in oscillation amplitude. When S rises, the fluid's

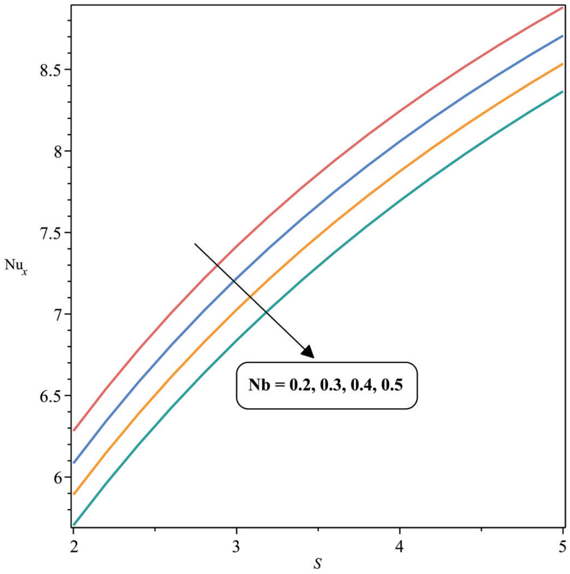

Figure 12. Consequence of Nb and S on Nu_x.

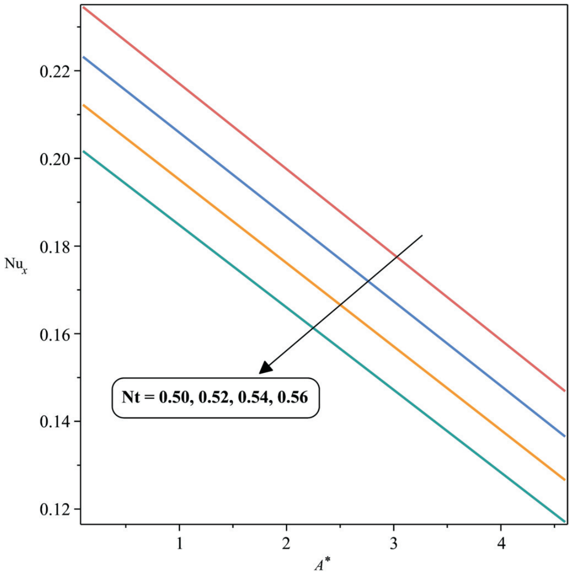

Figure 13. Consequence of Nt and A^* on Nu_x.

response becomes less efficient in transferring heat due to reduced fluid deformation and mixing. Similarly, the rise in Nb results in the suppression of heat transport by limiting the effective interface between particles and the liquid flow. These combined effects lead to a lower Nu_x, indicating less efficient heat transport. The influence of Nt and A^*

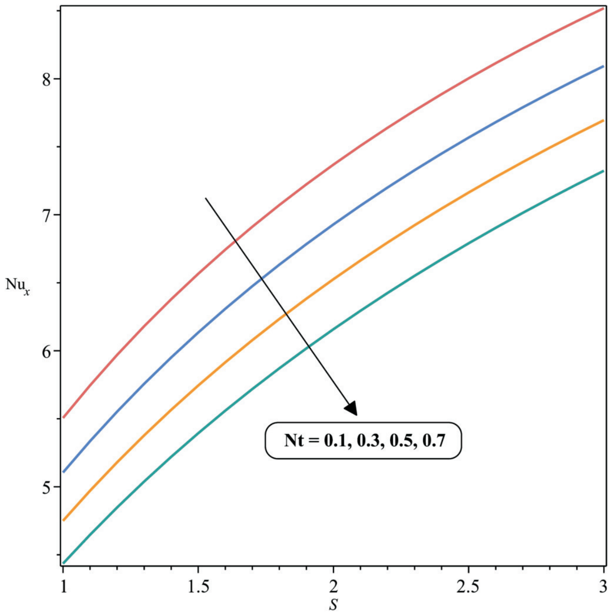

FIGURE 14. Consequence of Nt and S on Nu_x.

on the Nu_x is represented in Figure 13. The upsurge in values of Nt and A^* declines the Nu_x. This is due to the influence of Nt and A^* on the thermal boundary layer. As A^* rises, it causes more localized heating or cooling, reducing the thermal gradient and lowering the heat transport efficiency. Likewise, the intensification in Nt leads to the migration of particles due to temperature gradients, which reduces the effective heat transport rate by altering the flow attributes. As a result, Nu_x declines. The outcome of Nt and S on the Nu_x is represented in Figure 14. Here, the Nu_x reduces with an increase in Nt and S due to their effects on fluid flow and transmission. When S increases, it leads to more complex flow patterns, often resulting in less efficient heat transport by disrupting the temperature boundary layer and reducing the rate at which heat is transferred. Additionally, an elevation in Nt results in particle migration in fluid flow caused by temperature gradients, diminishing the effective heat transfer rate. Both factors together lower overall heat transfer, leading to a reduction in the Nu_x. For various $\tau\left(\frac{\pi}{2}, \pi, 2\pi\right)$ values, Table 1 depicts the values of Nu_x for several S and Table 2 portrays the values of Nu_x for several B^*. Table 3 represents the values of Sh_x for several τ and α values.

Deep neural network techniques are used inside the framework of PINNs to provide a unique approach for solving systems of PDEs. This method incorporates physical constraints into the model inherently by integrating functional approximations directly into the learning process. PINNs use deep neural architectures to solve both linear and nonlinear equations, in contrast to conventional numerical methods. With special attention to the function of automated differentiation in upholding governing physical laws and improving the interpretability of the underlying phenomena, the current paper offers a thorough examination of the PINN architecture and training methodology. Through a

Table 1. Values of Nu_x for several τ and S values.

Nu_x		S			
	τ	2	3	4	5
	$\frac{\pi}{2}$	0.315853	0.352602	0.378878	0.397706
	π	0.316856	0.330380	0.344927	0.358804
	2π	0.194393	0.228422	0.253326	0.274007

Table 2. Values of Nu_x for several τ and B^* values.

Nu_x		B^*			
	τ	0.2	0.4	0.6	0.8
	$\frac{\pi}{2}$	0.663479	0.611448	0.558642	0.505041
	π	0.553357	0.529787	0.505423	0.480223
	2π	0.123556	0.165807	0.206436	0.245535

Table 3. Values of Sh_x for several τ and α values.

Sh_x		α			
	τ	0.2	0.3	0.4	0.5
	$\frac{\pi}{2}$	0.763345	0.757018	0.750211	0.742880
	π	0.555704	0.547915	0.539447	0.530230
	2π	0.322955	0.311383	0.298580	0.284359

well-thought-out loss function, the model unifies beginning conditions, boundary conditions, and PDE residuals into a single formulation, thereby resolving the lack of data by guaranteeing conformity with the physical laws regulating heat transfer. Important hyperparameters that affect model performance and generalisation include learning rate, hidden-layer size, and regularisation strategies. These parameters need to be carefully adjusted to avoid overfitting while preserving accuracy. Iterative testing and validation are necessary because training length, which is based on the number of epochs, also has a significant impact on convergence behaviour and solution quality. This study applies the PINN model to the heat equation using 60,000 training epochs, a six-layer architecture with 72 neurons per layer, and a learning rate of 0.00001. Performance is assessed for a number of optimisers, such as Adam, gradient descent, and L-BFGS. Because of its second-order properties, L-BFGS is sensitive to local minima even if it converges more quickly than Adam. To increase convergence and decrease loss, a hybrid optimisation approach that combines Adam and L-BFGS is used.

Figures 15 and 16 show the expected temperature field and the distribution of absolute error (AE) along the fluid-flow geometry to demonstrate how the PINN captures spatial changes. The excellent agreement between anticipated temperature fields and actual expectations in these data shows that the PINN can successfully model heat transfer.

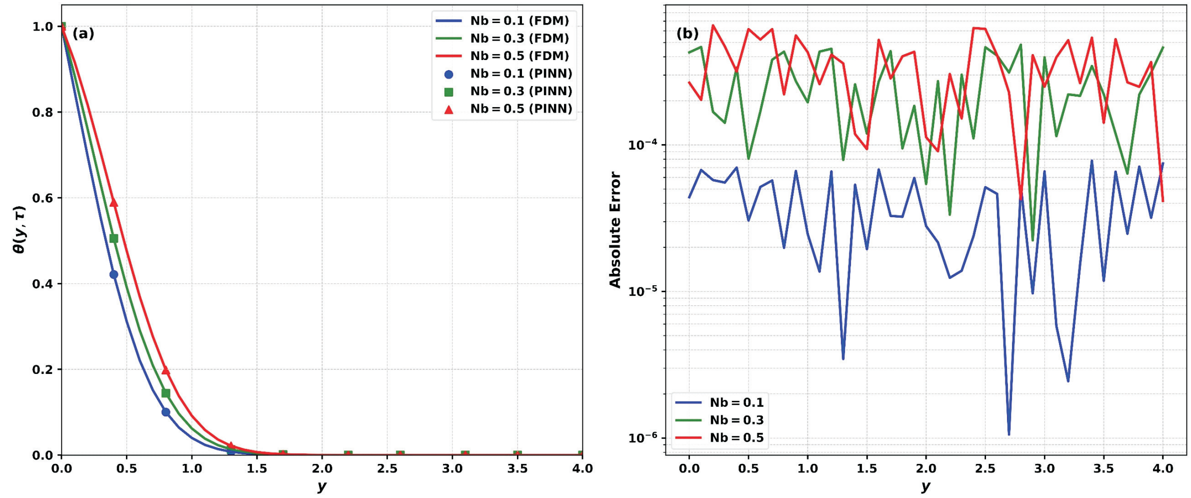

FIGURE 15. (a) Convergence of PINN results for $\theta(y,\tau)$. (b) AE of obtained PINN results.

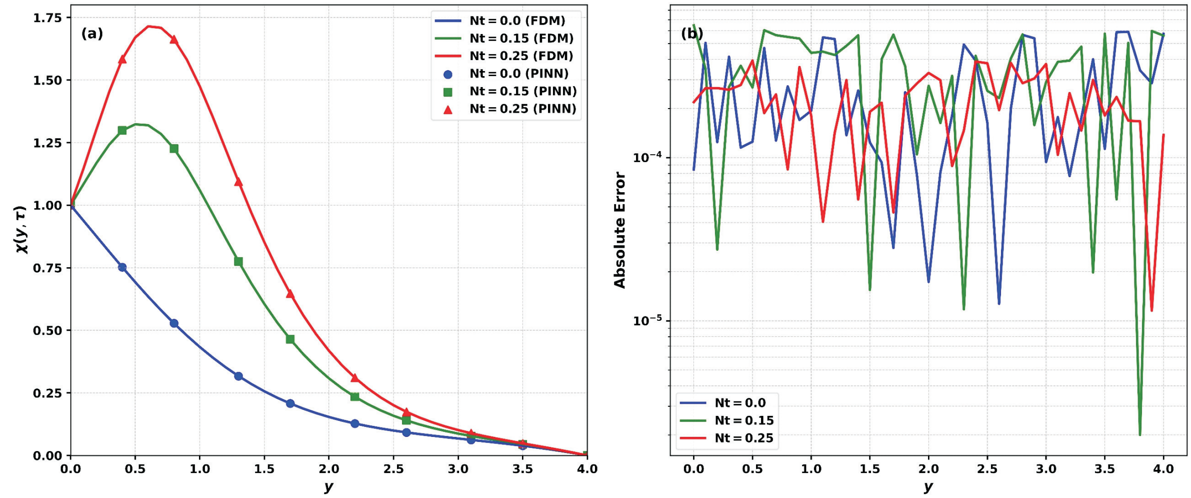

FIGURE 16. (a) Convergence of PINN results for $\chi(y,\tau)$. (b) AE of obtained PINN results.

According to the figures, temperature changes in the axial direction in a way that is consistent with how flow over the surface should behave. High prediction accuracy is shown by the AE values, which mostly fall between 10^{-4} and 10^{-6}. Localised complications like curvature effects or abrupt boundary interactions might be the cause of minor AE spikes at certain axial sites. Examining Figures 15(b) and 16(b) in further detail shows the model's generally low error levels in addition to its excellent spatial resolution. These subplots verify that, even in the vicinity of areas with nonuniform border features, the

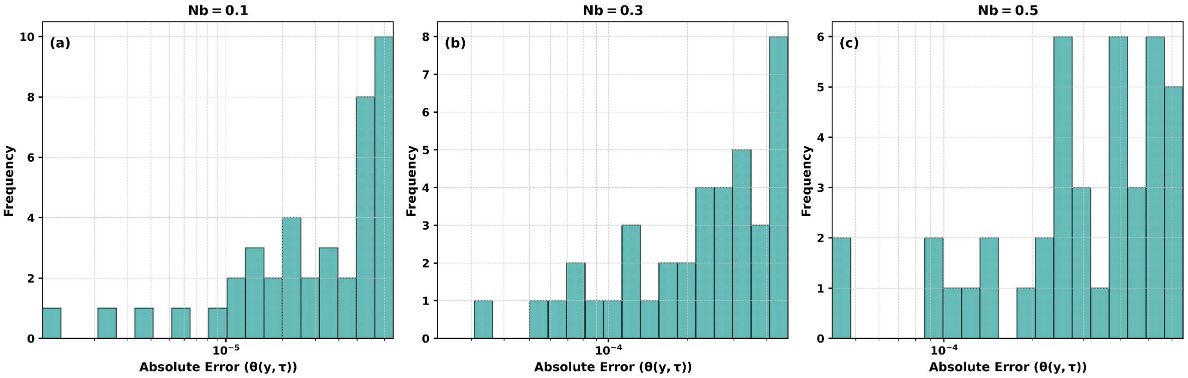

FIGURE 17. Illustration of error histograms for $\theta(y,\tau)$ obtained by PINN solutions.

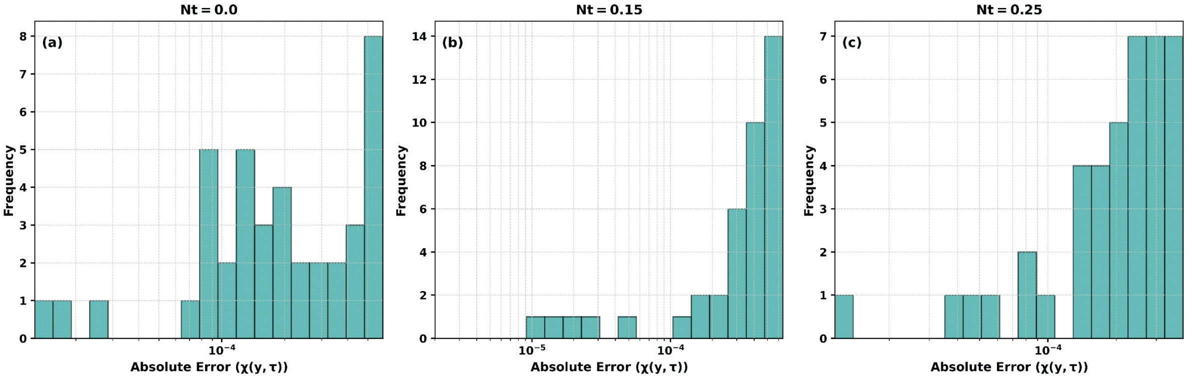

FIGURE 18. Illustration of error histograms for $\chi(y,\tau)$ obtained by PINN solutions.

AE stays bounded and does not exhibit any abnormal behaviour. The reliable results further imply steady network training and demonstrate how well automated differentiation works for calculating fractional and spatial derivatives in the physics-based loss formulation. The distribution of prediction mistakes is shown by error histograms in Figures 17 and 18. Strong precision and good agreement with the finite difference method (FDM) solution are shown by the concentration of values close to zero. Because the PINN model accurately depicts the controlling physics with little error fluctuations, it may be regarded as dependable for modelling thermal behaviour. The coefficient of determination (R^2) is used to further quantify the agreement between PINN forecasts and FDM findings. Several nondimensional temperature comparison situations are shown in Figure 19, with R^2 values ranging from 0.99 to 1.0 that are in agreement with the findings in each subplot. With R^2 ranging from 0.99 to 1.0, Figure 20 similarly shows the regression plots for $\chi(y,\tau)$. Clearly, the outstanding agreement between the FDM and PINN findings across a broad range of values is seen. Unlike classical numerical approaches that may

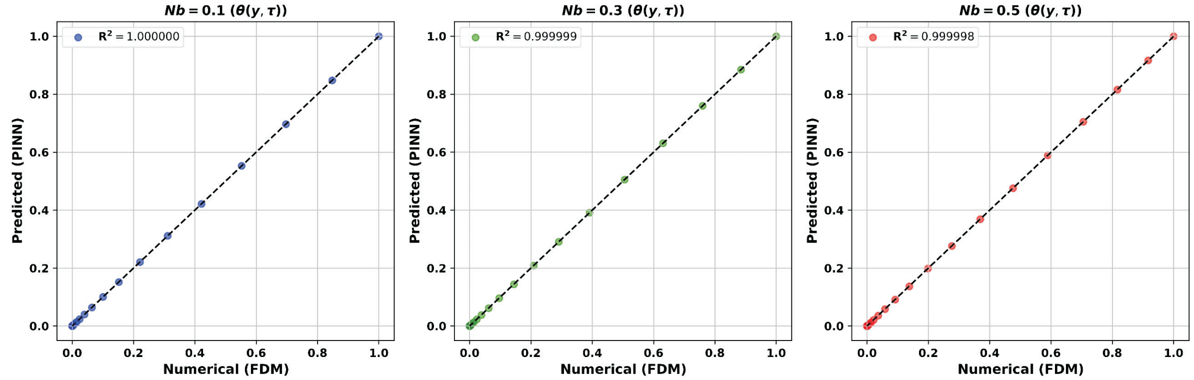

FIGURE 19. Regression plots for $\theta(y, \tau)$.

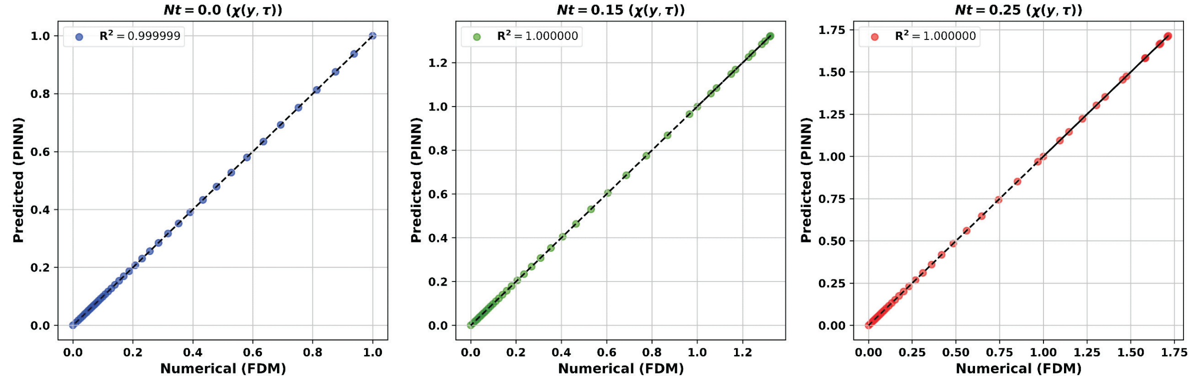

FIGURE 20. Regression plots for $\chi(y, \tau)$.

fail due to poor mesh quality or become computationally expensive at high resolution, the PINN framework provides a meshless alternative. Instead of depending on pointwise precise solutions at discrete time levels, it enforces the governing equations by minimising residuals over the domain.

6. Conclusion

The consequence of MF, non-uniform HSS, and TBM on the flow of liquid via an OSS in the existence of pollutant concentration is probed in the present study. This work adds to our knowledge of fluid behaviour and heat transmission in complicated systems. The oscillatory stretching sheet model may shed light on flow properties, boundary layer formation, and heat transfer processes, which are important in changing engineering uses such as material processing, cooling systems, and aeronautical engineering. Utilizing the similarity variables, the PDEs are altered to dimensionless equations. Moreover, the FDM is employed to crack the resultant equations numerically. The significance of numerous parameters on the involved profiles is established with the assistance of graphs. The main conclusion of the current investigation is given as follows,

- For various values of S, the Nusselt number Nu_x is enhanced approximately by 25.91% for $\tau = \frac{\pi}{2}$ and 13.23% for $\tau = \pi$.
- As the values of the S rise, the $\theta(y, \tau)$ reduces. When the ratio of the fluctuation rate to the extension rate is substantial, the fluctuating frequencies of the sheet increase more rapidly than the stretching rate.
- The $\theta(y, \tau)$ increases as the value of the Nb intensifies. An increased Nb may result in a reduced boundary layer and expedited heat transfer between the fluid and the stretched sheet due to improved mixing and thermal diffusion within the liquid.
- For various values of B^*, the heat transport rate is approximately about 31.37% for $\tau = \frac{\pi}{2}$ and 15.22% for $\tau = \pi$.
- The rise in values of Nt upsurges the thermal profile. The temperature gradually nears zero for extended durations as particles disperse throughout the fluid, a result of increased particle migration from the surface caused by the elevated thermophoresis parameter.
- The reduction in $\chi(y, \tau)$ can be seen as the Nb rises. The Nb often emerges from interactions with nanoparticles, correlating with an enhancement in Brownian motion.
- Good convergence is shown by the findings given by PINN and the solution originated by FDM. The minimal errors demonstrate that PINNs can successfully solve complex systems of PDE.

Industrial and environmental engineering significantly benefit from the study of fluid flow over an oscillatory stretched sheet with pollutant concentration. In manufacturing, such models facilitate the optimisation of coating and extrusion operations where fluids, including contaminants or additives, engage with dynamic surfaces, particularly in polymer processing, glass production, and metal rolling. In ecological engineering, these models facilitate the development of pollution control strategies by elucidating the dispersion of pollutants in air or aquatic environments influenced by oscillatory movements. They are also crucial in medical technology for the administration of medications via oscillating surfaces. Analysing the fluid dynamics and transfer of waste materials in stretched sheets may improve efficient garbage disposal and pollution mitigation strategies. Future scope is essential for formulating a research plan and any proposed project. Analysing past changes in the correlations between mass, thermal conductivity, and friction coefficients is crucial. Therefore, further investigation is needed to determine a generalised relationship between the hydrodynamic and thermal transport properties of an oscillatory stretched sheet. The results could be evaluated experimentally and quantitatively. In automobile radiators, many types of lead at high volume concentrations may be used as coolant. To enhance heat transfer and reduce friction, future studies could look into hybrid fluids made of multiple types combined in the same volume percentages.

Acknowledgments

The authors extend their appreciation to Umm Al-Qura University, Saudi Arabia for funding this research work through grant number: 26UQU4350370GSSR12. Also, the authors would like to thank the anonymous reviewers for their comments and suggestions.

Funding Statement

This research work was funded by Umm Al-Qura University, Saudi Arabia under grant number: 26UQU4350370GSSR12.

References

1. Z. Abbas, M. Imran and M. Naveed, *Time-dependent flow of thermally developed viscous fluid over an oscillatory stretchable curved surface*, Alexandria Engineering Journal, **59**(6) (2020), 4377–4390.
2. M. S. Abel and M. M. Nandeppanavar, *Heat transfer in MHD viscoelastic boundary layer flow over a stretching sheet with non-uniform heat source/sink*, Communications in Nonlinear Science and Numerical Simulation, **14**(5) (2009), 2120–2131.
3. K. S. Albalawi, K. Karthik, Mona Bin-Asfour, B. S. T. Alkahtani, J. Madhu, I. Alazman and R.J. Punith Gowda, *Impact of waste discharge concentration on fluid flow in inner stretched and outer stationary co-axial cylinders*, Applied Thermal Engineering, **244** (2024), Article Id: 122757.
4. N. Ali, S. U. Khan and Z. Abbas, *Unsteady Flow of Third Grade Fluid over an Oscillatory Stretching Sheet with Thermal Radiation and Heat Source/Sink*, Nonlinear Engineering, **4**(4) (2025), 223–236.
5. N. Ali, S. Ullah Khan, M. Sajid and Z. Abbas, *MHD flow and heat transfer of couple stress fluid over an oscillatory stretching sheet with heat source/sink in porous medium*, Alexandria Engineering Journal, **55**(2) (2016), 915–924.
6. B. Bhaumik, S. Changdar and S. De, *An Expert Model Based on Physics-Aware Neural Network for the Prediction of Thermal Conductivity of Nanofluids*, Journal of Heat Transfer, **144**(10) (2022), Article Id: 103501, 12 pages.
7. Y. S. Daniel, Z. Ismail, P. Ayuba, S. Daniel, P. Anthony, P. N. Okolo and A. S. Magaji, *Radiative heat transfer and Ohmic heating on unsteady EMHD mixed convective flow for dual stratified nanofluid*, Modeling Earth Systems and Environment, **11**(3) (2025), Article Number: 190, 19 Pages.
8. B. S. Goud and M. Aparna, *Radiation influence on unsteady MHD flow through a porous media past an infinite vertical plate in the presence of Dufour impact*, Modeling Earth Systems and Environment, **11**(5) (2025), Article Number: 377, 16 Pages.
9. T. Hayat, H. Ullah, B. Ahmad and M. Sh. Alhodaly, *Heat transfer analysis in convective flow of Jeffrey nanofluid by vertical stretchable cylinder*, International Communications in Heat and Mass Transfer, **120** (2021), Article Id: 104965.
10. T. Hayat, K. Muhammad and S. Momani, Melting heat and viscous dissipation in flow of hybrid nanomaterial: a numerical study via finite difference method, Journal of Thermal Analysis and Calorimetry, **147**(11) (2022), 6393–6401.
11. Z. Hussain, W. A. Khan, M. Ali, H. Shahid and M. Irfan, *Simultaneous features of nonuniform heat sink/source and activation energy in entropy optimized flow of Sutterby fluid subject to thermal radiation*, International Journal of Modern Physics B, **37**(21) (2023), Article Id: 2350208.
12. G. Jithender Reddy, V. V. L. Deepthi, R. Srinivasa Raju, B. Mallikarjuna Reddy and F. Ali, *Computational modelling of thermal and mass transport in MHD nanofluid flow across a non-linear surface with chemical response and viscous dissipation*, Modeling Earth Systems and Environment, **11** (2025), Article Number: 254, 12 Pages.
13. G. C. Kumar, K. J. Reddy, R. K. Konijeti and M. N. Reddy, *Non-Uniform Heat Source/Sink and Joule Heating Effects on Chemically Radiative MHD Mixed Convective Flow of Micropolar Fluid over a Stretching Sheet in Porous Medium*, Defect and Diffusion Forum, **388** (2018), 281–302.
14. I. E. Lagaris, A. Likas and D. I. Fotiadis, *Artificial neural networks for solving ordinary and partial differential equations*, IEEE Transactions on Neural Networks, **9**(5) (1998), 987–1000.
15. Y. Li, T. Liu and Y. Xie, *Thermal fluid fields reconstruction for nanofluids convection based on physics-informed deep learning*, Scientific Reports, **12**(1) (2022), Article number: 12567.
16. E. Lim, J. Chung, M. Sandberg and K. Ito, *Influence of chemical reactions and turbulent diffusion on the formation of local pollutant concentration distributions*, *Building and Environment*, **168** (2020), Article Id: 106487.
17. O. D. Makinde and T. Chinyoka, *Transient analysis of pollutant dispersion in a cylindrical pipe with a nonlinear waste discharge concentration*, Computers & Mathematics with Applications, 60(3) (2010), 642–652.

18. B. Manvi, J. Tawade, M. Biradar, S. Noeiaghdam, U. Fernandez-Gamiz and V. Govindan, *The effects of MHD radiating and non-uniform heat source/sink with heating on the momentum and heat transfer of Eyring-Powell fluid over a stretching*, Results in Engineering, **14** (2022), Article Id: 100435.
19. A. Merdasi, S. Ebrahimi, X. Yang and R. Kunz, *Physics Informed Neural Network application on mixing and heat transfer in combined electroosmotic-pressure driven flow*, Chemical Engineering and Processing-Process Intensification, **193** (2023), Article Id: 109540.
20. M. P. Mkhatshwa, S. S. Motsa and P. Sibanda, *MHD mixed convective radiative flow of Eyring-Powell fluid over an oscillatory stretching sheet using bivariate spectral method on overlapping grids*, Heat Transfer, **50**(1) (2021), 655–687.
21. D. K. Mohapatra, P. J. Camp and J. Philip, *Influence of size polydispersity on magnetic field tunable structures in magnetic nanofluids containing superparamagnetic nanoparticles*, Nanoscale Advances, **3**(12) (2021), 3573–3592.
22. S. R. Munjam, D. Gopal, N. Kishan, S. Formanova, K. Karthik, F. Ahmad, M. Waqas, M. Gupta and M. Ijaz Khan, *Brownian motion in a magneto Thermo-diffusion fluid flow over a semi-circular stretching surface*, Partial Differential Equations in Applied Mathematics, **12** (2024), Article Id: 100970.
23. M. Osaci and M. Cacciola, *A study of Brownian relaxation time in magnetic nanofluids: a semi-analytical model*, Multiscale and Multidisciplinary Modeling, Experiments and Design, **7** (2024), 15–29.
24. J. V. Ramana Reddy, V. Sugunamma and N. Sandeep, *Thermophoresis and Brownian motion effects on unsteady MHD nanofluid flow over a slendering stretching surface with slip effects*, Alexandria Engineering Journal, **57**(4) (2018), 2465–2473.
25. M. Z. Saghir and M. M. Rahman, *Brownian motion and thermophoretic effects of flow in channels using nanofluid: A two-phase model*, International Journal of Thermofluids, **10** (2021), Article Id: 100085.
26. P. Sharma, W. T. Chung, B. Akoush and M. Ihme, *A Review of Physics-Informed Machine Learning in Fluid Mechanics*, Energies, **16**(5) (2023), Article Id: 2343, 21 Pages.
27. F. A. Soomro, R. U. Haq and M. Hamid, *Brownian motion and thermophoretic effects on non-Newtonian nanofluid flow via Crank–Nicolson scheme*, Archive of Applied Mechanics, **91** (2021), 3303–3313.
28. Y-Q. Song, A. Hamid, T-C. Sun, M. I. Khan, S. Qayyum, R. Naveen Kumar, B. C. Prasannakumara, S. U. Khan and R. Chinram, *Unsteady mixed convection flow of magneto-Williamson nanofluid due to stretched cylinder with significant non-uniform heat source/sink features*, Alexandria Engineering Journal, **61**(1) (2022), 195–206.
29. P. Srilatha, K. Karthik, K. V. Prasad, A. Abdulrahman, R. S. Varun Kumar, R. J. Punith Gowda and R. Naveen Kumar, *Dynamics of Fourier's and Fick's laws on the convectively heated oscillatory sheet under Arrhenius kinetics: The finite-difference technique*, Journal of Computational Science, **82** (2024), Article Id: 102428.
30. T. Thumma, S. R. Mishra, M. A. Abbas, M. M. Bhatti and S. I. Abdelsalam, *Three-dimensional nanofluid stirring with non-uniform heat source/sink through an elongated sheet*, Applied Mathematics and Computation, **421** (2022), Article Id: 126927.
31. M. V. Varsha, B. N. Hanumagowda, K. M. Pavithra, Y. Jadeja, A. Kulshreshta, S. V. K. Varma, C. Prakash and K. Karthik, *Electromagnetic mixed convective flow of dusty hyperbolic tangent hybrid nanofluid over a stretching surface: A quadratic regression analysis using RSM*, International Journal of Thermofluids, **23** (2024), Article Id: 100803.
32. K. Vinutha, B. Shilpa K. V. Prasad, R. Naveen Kumar, R. J. Punith Gowda, T. Muhammad, R. Kumar and K. Karthik, *Concentration, Nanoparticle Diameter and Solid–Fluid Interfacial Layer on Nanofluid Flow Past a Convergent/Divergent Channel*, BioNanoScience, **14**(3) (2024), 2218–2227.
33. A. Ullah and S. Bilal, *3D flow of ternary nanofluid over non-linear surface by using surface response methodology with thermophoretic and Brownian aspects and by considering Xue and Yamada conductivity models*, Modeling Earth Systems and Environment, **11** (2025), Article Number: 288, 14 Pages.

34. M. Yaseen, S. K. Rawat, U. Khan, I. E. Sarris, H. Khan, A. S. Negi, A. Khan, E-S. M. Sherif, and A. Zaib, *Computational analysis of heat and mass transfer flow of wall jet hybrid nanofluid with irregular heat source/sink effects and waste discharge concentration*, Journal of Magnetism and Magnetic Materials, **588** (2023), Article Id: 171434.

G. J. Manjula, Department of Mathematics, Siddaganga Institute of Technology, Tumukuru-572 103, India.
Email address: `gjm@sit.ac.in`

Hakeem A. Othman, Department of Mathematics, Albaydha University, Albaydha, Yemen.
Email address: `hakim_albdoie@yahoo.com`

S. Suresha, Department of Physics, Government first Grade College, Santhebennur-577 552, Karnataka, India.
Email address: `sureshafgc@gmail.com`

Husniyah Alzubaidi, Department of Mathematics, AL-Qunfudhah University college, Umm Al-Qura University, Kingdom of Saudi Arabia.
Email address: `hazbaidi@uqu.edu.sa`

A. B. Sathisha, Department of Mathematics, Government First Grade College, Jagalur-577 528, Davanagere, Karnataka, India
Email address: `sathishaab@gmail.com`

C. G. Jagannatha, Department of Mathematics, HPPC Government First Grade College, Challakere-577 501, Karnataka, India.
Email address: `cgjagannath@gmail.com`

Lal Sing Naik, Department of Mathematics, Government Science College, Chitradurga-577 501, Karnataka, India.
Email address: `lsnaikchiru@gmail.com`

K. C. Jagadeesha, Department of Mathematics, Government First Grade College, Tumkur-572 102, Karnataka, India.
Email address: `kcjagadish.09@gmail.com`